

LongAxis: a MATLAB-based program for 3D quantitative analysis of epithelial cell shape and orientation

Keith R. Carney, Chase D. Bryan, Hannah B. Gordon, and Kristen M. Kwan

Department of Human Genetics
University of Utah, Salt Lake City, UT 84112

Corresponding author:

Kristen M. Kwan
Department of Human Genetics
EIHG 5100
University of Utah
15 North 2030 East
Salt Lake City, UT 84112
phone: 801-585-7541
fax: 801-581-7796
email: kristen.kwan@genetics.utah.edu

Running Title: LongAxis for 3-dimensional quantitative analysis of optic cup organization

Keywords:

Bullet Points:

Grant Sponsor and Number:

1 **Abstract**

2 Epithelial morphogenesis, a fundamental aspect of development, generates 3-dimensional
3 tissue structures crucial for organ function. Underlying morphogenetic mechanisms are, in
4 many cases, poorly understood, but mutations that perturb organ development can affect
5 epithelial cell shape and orientation – difficult features to quantify in three dimensions. The
6 basic structure of the eye is established via epithelial morphogenesis: in the embryonic optic
7 cup, the retinal progenitor epithelium enwraps the lens. We previously found that loss of the
8 extracellular matrix protein *laminin-alpha1 (lama1)* led to mislocalization of apical polarity
9 markers and apparent misorientation of retinal progenitors. We sought to visualize and quantify
10 this phenotype, and determine whether loss of the apical polarity determinant *pard3* might
11 rescue the phenotype. To this end, we developed LongAxis, a MATLAB-based program
12 optimized for the retinal progenitor neuroepithelium. LongAxis facilitates 3-dimensional cell
13 segmentation, visualization, and quantification of cell orientation and morphology. Using
14 LongAxis, we find that retinal progenitors in the *lama1^{-/-}* optic cup are misoriented and slightly
15 less elongated. In the *lama1;MZpard3* double mutant, cells are still misoriented, but larger.
16 Therefore, loss of *pard3* does not rescue loss of *lama1*, and in fact uncovers a novel cell size
17 phenotype. LongAxis enables population-level visualization and quantification of retinal
18 progenitor cell orientation and morphology. These results underscore the importance of
19 visualizing and quantifying cell orientation and shape in three dimensions within the retina.

20

21

22 **Introduction**

23 Organogenesis requires assembly of cells into precise 3-dimensional structures which are
24 crucial for function. Disruptions to this morphogenetic process can lead to organ dysfunction,
25 and are a common cause of birth defects. Cellular and molecular mechanisms governing organ
26 morphogenesis are generally not well understood: many signals and pathways have been
27 identified, often on the basis of genetic studies and mutant phenotypes. Despite this, analyzing
28 genetic interactions and dissecting how different factors impact morphogenesis has been a
29 challenge, since, in many cases, it has not been trivial to visualize and quantify phenotypes in
30 three dimensions.

31 The vertebrate eye forms via a complex morphogenetic process, during which the optic
32 vesicle, an outpocketing of the forebrain, undergoes cell and tissue movements to become the
33 optic cup, in which the hemispherical retina enwraps the lens. At the end of optic cup
34 morphogenesis, the retinal epithelium is comprised of progenitor cells which are elongated and
35 oriented toward the lens. In fish, mouse, and chick, genetic screens, candidate approaches,
36 and conditional genetic studies have identified factors involved in optic cup tissue organization
37 (Adler and Canto-Soler, 2007; Bazin-Lopez et al., 2015; Chow and Lang, 2001; Fuhrmann,
38 2010; Martinez-Morales and Wittbrodt, 2009; Yang, 2004). One key factor governing optic cup
39 tissue organization and morphogenesis is the extracellular matrix, a complex proteinaceous
40 layer that surrounds epithelial tissues and provides polarity, survival, and signaling cues (Adams
41 and Watt, 1993; Daley and Yamada, 2013; Frisch and Francis, 1994; Juliano et al., 2004;
42 Martin-Belmonte and Mostov, 2008). It has long been known that a complex extracellular matrix
43 layer surrounds the nascent developing eye of all vertebrate species examined to date (Hendrix
44 and Zwaan, 1975; Hilfer and Randolph, 1993; Kwan, 2014; Parmigiani and McAvoy, 1984;
45 Peterson et al., 1995; Svoboda and O'Shea, 1987; Tuckett and Morriss-Kay, 1986; Wakely,
46 1977; Webster et al., 1984), and functional roles for specific extracellular matrix molecules in
47 early eye development are starting to be resolved using molecular genetic approaches (Bryan et

48 al., 2016; Hayes et al., 2012; Huang et al., 2011; Lee and Gross, 2007; Semina et al., 2006).
49 We previously found that loss of *laminin-alpha1* (*lama1*) results in disruption of tissue polarity
50 and cellular disorganization within the retinal epithelium of the zebrafish optic cup (Bryan et al.,
51 2016). At the single-cell level, retinal progenitors appeared misoriented, although this seemed
52 variable between individual mutant embryos and was largely inferred by scanning through
53 volume data (z-stacks acquired by confocal microscopy). In addition to the tissue
54 disorganization defect, the *lama1* mutant displayed ectopic localization of the apical marker
55 *pard3* at inappropriate locations, including what would normally be the basal surface of the optic
56 cup. We wondered whether the establishment of ectopic apical surfaces might cause the
57 disorganization phenotype, and whether removal of the apical determinant *pard3* could rescue
58 it.

59 Although we had questions, we lacked the methodology to adequately and quantitatively
60 analyze such phenotypes. We were not previously able to visualize or quantify cell orientation
61 in 3-dimensions, phenotypic variability between embryos, nor how changes in cell shape or
62 volume might contribute to mutant phenotypes. With these goals in mind, we have developed
63 LongAxis, a MATLAB-based program which allows us to qualitatively and quantitatively assay
64 multiple aspects of cell morphology and organization, optimized for the developing retina. Using
65 a combination of automated segmentation and refinement (or filtering) via user selections to
66 remove outliers and incompletely segmented cells, we can visualize and analyze cell orientation
67 and shape in 3-dimensions throughout the tissue. Cell orientation, length, length/width ratio,
68 and cell volume can be calculated for thousands of cells simultaneously; these features can be
69 displayed in the intuitively simple “urchin plot”, which conveys the cell’s extent of elongation
70 (length/width ratio) and orientation.

71 Using LongAxis, we finally resolved questions regarding the *lama1* mutant optic cup
72 phenotype, including how cell orientation and morphology are quantitatively affected, and
73 whether genetic removal of the apical polarity determinant *pard3* is able to rescue it. We find

74 that in the *lama1* mutant optic cup, retinal progenitors are indeed misoriented, and that
75 misoriented cells cluster together in domains. Cells are shorter and less elongated, but not
76 smaller than wild type cells. In the *lama1;MZpard3* double mutant, retinal progenitors are still
77 misoriented, and we uncover a cellular-level phenotype: cells are larger than either wild type or
78 *lama1* single mutants. Therefore, loss of *pard3* does not rescue the *lama1* mutant tissue
79 organization phenotype. Importantly, rather than 2-dimensional measurements in a small
80 number of sparsely labeled cells, LongAxis allows us to discover population-level alterations in
81 cell morphology and organization, and underscores the importance of quantitative analysis of
82 cellular level phenotypes.

83

84 **Results**

85 *Pipeline for 3-dimensional cell segmentation*

86 Our goal is to understand the molecular basis of cell and tissue organization within the
87 embryonic optic cup. Although many factors have been identified as playing a role in this
88 process, our analysis has largely been limited to 2-dimensional analysis of a small sampling of
89 cells. Dissecting genetic interactions and mechanisms would ideally be carried out by
90 quantitatively evaluating cell orientation and morphology throughout the retinal progenitor cell
91 population. To this end, we developed LongAxis, a program to facilitate visualization and
92 quantification of cell morphology within the zebrafish optic cup.

93 The goal of this software is accurate single cell segmentation and automated quantitative
94 analysis of cell shape and orientation within the context of the tissue, therefore, a crucial initial
95 optimization step is obtaining image data of adequate quality. To avoid distortion and changes
96 in volume that accompany tissue fixation, we imaged live embryos at optic cup stage (24 hours
97 post fertilization (hpf) in zebrafish), in which all membranes were labeled using EGFP-CAAX.
98 Images were acquired at 1024x1024 resolution, and we aimed for adequate axial sampling

99 without photobleaching, deciding upon a voxel size of 0.21x0.21x0.42 μm (x:y:z ratio of 1:1:2;
100 Movie 1).

101 In LongAxis, cell segmentation begins with eight steps of 2D processing applied to every
102 slice, with the goal of enhancing boundaries (Figure 1B; see also Methods, LongAxis MATLAB
103 code). The processing steps outlined here are optimized for our specific data sets, the goal
104 being to visualize and analyze retinal epithelial cells. In our experience, the key step was to
105 correct for variations in signal (i.e. some regions of membrane around any particular cell might
106 be brighter or dimmer than others) in order to ensure that the cells were segmented along
107 membrane boundaries accurately. Once 2D processing has been carried out, the user selects
108 the 3D volume of interest within the image data for 3D segmentation and rendering. In our
109 case, this focuses our analysis on the retinal epithelium and excludes cells outside, such as
110 prospective brain, lens, and overlying ectoderm. Once the subvolume of interest has been
111 selected, 3D processing functions are applied to enhance and connect boundaries across slices
112 (Figure 1C). This initially yields 3D cell segmentation throughout the volume data (Figure 1D,
113 E). The 3D cell segmentation is then applied within the user-selected subvolume, leaving only
114 cells within the region of interest (Figure 1F-H). Segmentation can be examined in small
115 volume regions for visual validation at this stage (Figure 1I-J; Movies 2, 3).

116 Following this, the set of segmented cells is refined: cell segmentation needs to be
117 validated, and unwanted cells, particularly those in which segmentation failed, are removed from
118 the data set. To this end, a process of “informed filtering” is carried out (Figure 1A). The basic
119 idea is to validate cell shapes in a manner unbiased with respect to the orientation of the cell;
120 assaying changes in cell orientation is a major goal of this software. To carry out filtering, an
121 expert user (i.e. someone experienced with looking at these data) views 3-dimensional
122 segmented cell shapes (away from the image data), and manually validates cells which appear
123 to have a retinal epithelial morphology. If need be, the user can cross-check the position of the
124 cell to ensure that cells within the retinal epithelium are being selected, or the user can also

125 check the cell rendering against the original image data. The ability to cross-check may be
126 useful in cases (e.g. mutants) where cell morphologies could be dramatically altered, but again,
127 the basic idea is to carry out these selections in an unbiased manner with respect to position
128 and orientation of the cell within the tissue.

129 Once the user has selected cells, the user-selected data set is analyzed: minimum and
130 maximum values for cell volume, length, and length/width ratio are derived. These
131 minimum/maximum (min/max) values for these three criteria are applied to refine and filter the
132 entire data set (all segmented cells in the region of interest); this process thereby excludes
133 “outlier” cells with respect to these three specific criteria. The filtered cell set, which represents
134 all retinal epithelial cells (selected in an unbiased manner) is used for quantitative analysis of
135 cell morphology and orientation and 3-dimensional visualization.

136

137 *LongAxis analysis and outputs*

138 Once cells are segmented, a variety of outputs can be acquired, including 3-dimensional
139 visualization of cell shape, and quantitative outputs including cell length, cell width, length/width
140 ratio (a metric of how elongated the cell is), and cell orientation (Figure 2A-D; Movie 4). Cell
141 orientation is quantified within the 3-dimensional tissue by deriving the cell convergence point:
142 the average of all midpoints of closest approach for all cell orientation vector pairs (Figure 2E;
143 Movie 5). This was empirically derived for each embryo independently: we found that existing
144 landmarks (e.g. the lens center of mass) incurred too much variability between embryos, as lens
145 shape, size, and even position can vary slightly with respect to the retinal epithelium. Once the
146 vector convergence point is obtained, the long axis, which is derived from the ellipsoid fit, is
147 used to calculate an angle of deviation (or deflection) from that convergence point for each cell
148 (Figure 2F, marked by red asterisk). In addition to the quantitative output, angles of deviation
149 and length/width ratio can all be represented in an “urchin plot”, a 3-dimensional visual
150 representation of cell orientation and shape within the tissue (Figure 2G). In the urchin plot, the

151 angle of deviation is represented by a heat map, in which close adherence to the expected
152 angle is coded in bluer colors, and significant deviation is encoded by warmer colors. The
153 length of the vector is proportional to the length/width ratio of the cell, to represent one aspect of
154 cell shape.

155

156 *Validating segmentation and filtering*

157 To determine how well the workflow performs, segmentation and filtering validation steps
158 were carried out on three independent subregions of the image volume data (one example in
159 Figure 3A). First, because segmented cell shapes were initially viewed in an isolated manner,
160 away from the image data, we visually examined all segmented cells in each subregion against
161 the original image data. We used xy, xz, and yz cutaways to evaluate how well the
162 segmentation matched the membrane signal, including whether the process correctly
163 segmented single cells. Segmentation accuracy for all cells was scored manually (by a user) on
164 a scale of 1-5, with 1-4 corresponding to how well the segmentation matched the membrane
165 boundaries in the image data (1 = 90-100% matching boundaries; 2 = 70-90%; 3 = 50-70%; 4 =
166 <50%), and a score of 5 representing unsuccessful segmentation resulting in fused cells.
167 Despite presence of some variability in rendering quality, cell orientation was largely unaffected
168 for cells in categories 1-3. The proportions of cells in each category is shown in Figure 3B.

169 We then asked how filtering (using parameters derived from user selections for cell volume,
170 cell length, and length/width ratio) affected the number of cells in each group. We examined the
171 subset of cells that passed the filtering criteria, and we found that indeed, although filtering is
172 not perfect, poorly segmented (class 4) and fused cells (class 5) are preferentially removed from
173 the filtered data set (Figure 3B; number of cells removed from each class 1-5, in order: 3, 5, 2,
174 12, 13). These analyses suggest that the segmentation identifies cells in 3-dimensions and
175 filtering helps to remove unsuccessfully segmented cells, leaving us with a data set appropriate
176 for population-level quantitative analysis.

177

178 *Determining filter parameters and the size of the user-selected data set*

179 Accurate filtering relies on having a set of cells selected by an expert user; filtering
180 parameters are derived from this user-selected cell set. How many cells does the user need to
181 choose to generate reliable filtering parameters? We tested this in 4 different wild type embryos
182 by examining the relationship between number of cells selected and number of cells filtered out,
183 the rationale being that as the number of selected cells increases, more reliable filter
184 parameters will be generated. This, however, only works up to a point at which selecting more
185 cells has no more benefit; the user set will have already captured the full range of appropriately
186 segmented cells. We find that the relationship between number of cells selected and number of
187 cells filtered out obeys exponential decay (Figure 3C; Figure S1A); deriving the equation to
188 describe this graph allows us to easily calculate the number of cells which need to be selected
189 to carry out filtering (using the mean lifetime equation $\tau = \lambda^{-1}$, where λ is the decay rate and τ
190 represents the mean lifetime, or here, the average number of selections it takes to remove a
191 cell). For the 4 wild type embryos examined, although substantial numbers of cells were
192 manually selected by the user (1269, 1788, 2420, and 1582, respectively), significantly fewer
193 cells (using the mean lifetime equation to solve for τ : 253, 119, 120, and 61, respectively)
194 needed to be selected in order to exclude the inappropriately segmented cells without
195 inappropriately removing correctly segmented cells (Figure 3C; Figure S1A). While the number
196 of user-selected cells necessary for adequate filtering needs only to be a small proportion of the
197 total number of cells, filtering quality clearly increases with more user-selected and validated
198 cells. In addition, the derived equation reveals that there is a minimum of cells that will be
199 excluded in each wild type embryo (using the exponential decay equation (see Methods) and
200 solving for y_i : 192, 132, 200, and 515, respectively); based on our manual validation, these are
201 likely to represent poorly segmented and fused cells. We think the variability in this number

202 between embryos is due to variation in image quality, which will affect the success of the
203 segmentation process.

204 This post hoc analysis reveals that there is not one single baseline number of cells for a
205 user to select, however, the software is simple to use, and selecting a few hundred cells will
206 likely yield high quality filtering information necessary to remove unwanted cells.

207

208 *Filtering poorly segmented cells does not change the data set*

209 Given that filtering does change the number of cells being used for quantitative analysis
210 (Table 1), we asked how it might alter, at the population level, the quantitative measurements of
211 interest: angle of deviation, cell length, length/width ratio, and volume (Figure 3D-G; Figure
212 S1B-E). We find that in the cases of angle of deviation, cell length, and length/width ratio, the
213 distributions of filtered cells are not altered from the original (full) set of segmented cells (Figure
214 3D-F; Figure S1B-D, letters in graphs (A, B) represent different statistical groups). In contrast,
215 cell volume is changed such that the filtered set is not statistically different from the user
216 selections (Figure 3G; Figure S1E), consistent with the idea that inappropriately segmented,
217 and especially fused cells (which are larger) are removed from the filtered data set. Importantly,
218 distributions of orientation angles do not change (Figure 3D; in 3 out of 4 wild type embryos,
219 two-sample Kolmogorov-Smirnov tests show no significant difference between the set of all
220 segmented cells and the filtered set), so filtering would not influence large-scale analysis of cell
221 orientation and tissue organization. We conclude from these analyses that filtering works to
222 preferentially remove outlier cells, without changing the population distribution of the data with
223 respect to cell length, length/width ratio, and angle of deviation.

224

225 *Wild type embryos exhibit slight morphological variability between cell populations*

226 With our new tool in hand, we first set out to examine multiple wild type embryos to
227 determine the amount of variability we might detect between samples of the same genotype.

228 Development in zebrafish is not deterministic, and we expect there to be some variability
229 between individuals with respect to eye size and cell number. To examine this, four different
230 wild type embryos were imaged and analyzed using the LongAxis pipeline, with filtering
231 parameters and cell convergence points derived independently for each individual embryo
232 (Figure 4A-A''', Movie 6). In Movie 6, isosurfaces show highest density regions of midpoints of
233 closest approach for all pairwise vector combinations, and black dot shows the derived
234 convergence point (the average of all calculated midpoints) which was used for angle of
235 deviation measurements. Urchin plots were generated to visualize cell orientation in a
236 qualitative manner (Figure 4B-C''', Movie 7), and at this level of resolution, the optic cups exhibit
237 some variation in size and shape (including lens shape). Despite this, the cells (represented as
238 vectors in the urchin plot) largely appear to be aligned toward the calculated convergence point
239 (labeled as colors in the blue range in the heat map), with the reproducible exception of the
240 optic fissure opening at the ventronasal side of the eye (Figure 4B-C''', asterisks). These data
241 are represented quantitatively as a density plot of angles of deviation (Figure 4D); the
242 distributions of angles of deviation appear similar between the four embryos, with a peak $\sim 20^\circ$.
243 Quantitative analysis and comparison of these 4 wild type embryos reveals other notable
244 features. First, the numbers of retinal epithelial cells vary between the optic cups (1824, 2413,
245 3752, and 2019, respectively; Table 1), but these numbers are in the same range as previously
246 calculated using a completely independent method which relied on counting nuclei (Kwan et al.,
247 2012). This serves as a convenient independent validation of our approaches. Next, the
248 distributions of cell length and volume appear different, but fall only into two statistical groups
249 (Figure 3E, G; mean length (μm): 16.26, 15.9, 16.29, 16.59; mean volume (μm^3): 346.28,
250 305.28, 337.3, 341.05). There is no significant difference in cell length/width ratio between the
251 four embryos (Figure 3F; mean length/width ratio: 2.06, 2.08, 2.09, 2.1). Taken together, these
252 data indicate that the quantitative analysis can distinguish between individual embryos of the

253 same genotype, due to normal phenotypic variability; therefore, multiple embryos must be used
254 to compare different experimental conditions and genotypes.

255

256 *Putting the software to the test: genetics of apicobasal polarity and tissue organization in the*
257 *optic cup*

258 Having determined that we could segment cells and carry out quantitative analysis on cell
259 morphology and orientation, we turned our attention to the original biological question at hand.
260 We previously demonstrated that loss of *lama1* leads to disruptions to epithelial polarity and
261 apparent disorganization of the retinal progenitor epithelium (Bryan et al., 2016). Although we
262 hypothesized that the cause of this phenotype was cell misorientation as opposed to gross
263 changes in cell size or shape, we had no way at the time to visualize or quantitatively test this.
264 In addition to the retinal disorganization, we found that tissue polarity is disrupted in *lama1*
265 mutants: apical markers such as *pard3* are mislocalized and even ectopically localized to
266 subcellular locations that would, in a wild type embryo, be the basal surface. We wondered
267 whether ectopic localization of apical determinants was the cause of the structural
268 disorganization in the *lama1* mutant optic cup, and therefore, whether the *lama1* mutant
269 phenotype might be rescued by genetic removal of *pard3*.

270 With LongAxis in hand, we set out to answer these questions. We generated double
271 mutants for *lama1* and *pard3*, in which *pard3* was both maternally and zygotically lost
272 (*lama1;MZpard3*), as *pard3* is maternally loaded (Blasky et al., 2014). We compared wild type
273 optic cups to the *lama1* single mutants and the *lama1;MZpard3* double mutants. When initially
274 viewing single optical sections of all three genotypes (Figure 5A-A''), the *lama1* single mutant
275 exhibits the expected disorganized retinal epithelium with cells that appear cuboidal in cross
276 section (Figure 5A', Movie 8). The *lama1;MZpard3* optic cup initially appeared as though the
277 disorganized retinal progenitor cell phenotype might be partially rescued (Figure 5A'', Movie 9);
278 in this optical section, some cells are elongated and oriented toward the lens.

279 This, however, underscores the importance of our approach, as 3-dimensional visualization
280 and quantification are necessary to actually resolve whether the phenotype is rescued or not.
281 Three independent embryos of each genotype (*lama1*^{-/-} and *lama1*^{-/-};*MZpard3*^{-/-}) were imaged,
282 processed through our LongAxis pipeline, and compared to the wild type optic cups. First, cell
283 convergence points were derived (Movie 10) and urchin plots were generated to qualitatively
284 visualize and compare cell orientation (Figure 5B-C''; Movies 11, 12). Because of the heat map
285 coding of the vectors, it is intuitively clear that significant regions of the optic cup in both *lama1*
286 and *lama1*;*MZpard3* double mutant eyes are comprised of misoriented cells. Substantial
287 patches of the urchin plots are populated by vectors in the red-orange-yellow range, indicating
288 an angle of deviation >60°. Interestingly, misoriented cells were found clustered, as opposed to
289 individually randomly scattered throughout the eye.

290 This is also represented quantitatively in the angle of deviation density plots (Figure 5D-D''):
291 the four wild type embryos all have a peak ~20°, indicating a small deviation from the
292 convergence point, and a small trailing tail out beyond 60° (Figure 5D; Movie 7). In contrast, the
293 *lama1* single mutants show a very different distribution in angles of deviation: in one embryo,
294 there is a visible peak ~20°, similar to wild type embryos, but in the other two embryos, there is
295 no clear peak, rather, angles of deviation are distributed more evenly from 20-90° (Figure 5D';
296 Movie 11). Similarly, all three *lama1*;*MZpard3* double mutants show an even distribution of
297 angles of deviation from 20-90°, without a clear peak (Figure 5D''; Movie 12). This indicates that
298 at the population level, cells are significantly misoriented in both the *lama1* single mutant and
299 *lama1*;*MZpard3* double mutant optic cups.

300 In our previous work, we quantified morphology of a small number of cells to determine
301 whether tissue disorganization might actually be caused by changes in cell length or
302 length/width ratio. Assaying limited numbers of cells primarily in 2 dimensions, we found that
303 retinal progenitor cell length was diminished, but length/width ratio was unaffected (Bryan et al.,

2016). Although we had obtained a preliminary answer to our question, we wanted to determine if these trends held true with more thorough quantification of cell morphology across the population of retinal progenitors.

Using our LongAxis pipeline, we compared retinal progenitor cell length, length/width ratio, and volume at the population level, with >1000 cells per eye. First, in terms of cell length (Figure 5E-E’), we find that *lama1* mutant retinal progenitor cells are shorter than wild type; this is consistent with our previous data (Bryan et al., 2016). In contrast, however, *lama1;MZpard3* double mutant retinal progenitor cell length is indistinguishable from wild type (wild type $16.25 \pm 4.77 \mu\text{m}$; *lama1*^{-/-} $15.92 \pm 5.04 \mu\text{m}$; *lama1*^{-/-};*MZpard3*^{-/-} $16.19 \pm 4.97 \mu\text{m}$). Next, we examined length/width ratio: although our previous 2-dimensional analysis indicated that length/width ratio was unaffected by loss of *lama1* in our small sampling of cells, our 3-dimensional analysis demonstrates that loss of *lama1* or loss of both *lama1* and *pard3* leads to diminished length/width ratio (Figure 5F-F’; wild type 2.08 ± 0.50 ; *lama1*^{-/-} 2.03 ± 0.55 ; *lama1*^{-/-};*MZpard3*^{-/-} 1.97 ± 0.39). The difference between wild type and *lama1* mutants appears subtle but is significant, likely due to the large numbers of cells measured. Finally, we assayed retinal progenitor cell volume: loss of *lama1* does not affect retinal progenitor cell volume, however, *lama1;MZpard3* double mutant cells are larger than either wild type or *lama1* single mutant (Figure 5G-G’; wild type $331.97 \pm 183.42 \mu\text{m}^3$; *lama1*^{-/-} $333.86 \pm 201.88 \mu\text{m}^3$; *lama1*^{-/-};*MZpard3*^{-/-} $369.94 \pm 229.80 \mu\text{m}^3$).

Taken together, these measurements are a rich source of quantitative information from which to draw a number of conclusions. First, there is variability in the *lama1* mutant misorientation phenotype. We had previously observed this, but did not have a way to quantify it. Mutant embryos can display varying degrees of tissue disorganization, potentially due to the degree to which the cells might self-organize (possibly influenced by aberrant localization of apical polarity complexes) in the absence of extrinsic polarity cues from laminin. Second, although cell size and shape are slightly different in the *lama1* single mutant compared to wild

330 type, change in cell morphology is unlikely to be the cause of the misorientation phenotype. In
331 contrast, the *lama1;MZpard3* double mutant has larger, less elongated cells (greater volume,
332 diminished length/width ratio). Finally, and importantly, at the population level, retinal progenitor
333 cells in *lama1* single mutants and *lama1;MZpard3* double mutants are dramatically misoriented
334 compared to wild type. Despite the appearance of partial rescue in a single optical section
335 (Figure 5A-A''), these data clearly demonstrate that loss of *pard3* does not rescue the tissue
336 disorganization phenotype in the *lama1* mutant. These 3-dimensional visualization and
337 quantitative analyses underscore the utility of our approach.

338

339

340 **Discussion**

341 A key part of epithelial organogenesis is the establishment of tissue-specific structures
342 which are crucial for eventual organ function. Within these epithelial tissues, cells take on a
343 stereotypical 3-dimensional organization. Much work has gone into identifying molecular
344 signals and pathways that influence this organization. The vertebrate eye is a somewhat unique
345 structure, in which the hemispherical retinal epithelium enwraps the lens. We originally set out
346 to determine how changes in one such class of molecules, the extracellular matrix, affect tissue
347 organization: previously, we found that loss of *lama1* leads to disruptions to tissue polarity and
348 apparent disorganization of the retinal epithelium. 2-dimensional analysis of a limited sampling
349 of cells suggested that cell length was shorter, but length-width ratio seemed unaffected. In
350 addition, loss of *lama1* resulted in ectopic localization of the apical determinant *pard3* and other
351 apical markers, and we wondered whether loss of *pard3* could rescue these phenotypes. Due
352 to limitations in our ability to visualize and quantitatively analyze 3-dimensional cell shape and
353 orientation, we were not able to test this until now.

354 LongAxis allows us to take volume data (e.g. confocal z-stacks that are simple to acquire for
355 zebrafish embryos), and run it through a 3-dimensional cell segmentation and analysis pipeline,

356 which includes manual cell selections and filtering based on parameters derived from the
357 manually selected cells. After filtering, LongAxis provides intuitive visualization (in the form of
358 the “urchin plot”) and quantitative analysis of cell orientation and a number of cell morphology
359 descriptors, including length, width, length-width ratio, and volume. The power of LongAxis is in
360 the ability to analyze cell shape and organization at the population level – thousands of cells per
361 eye – rather than manually measuring 2-dimensional features on a limited sampling of cells.
362 This allows us to examine distributions within the cell population as well as variability between
363 individual embryos.

364 Using LongAxis, we validated our pipeline via manual validation of segmentation and
365 filtering, finding that filtering preferentially removes poorly and incompletely segmented cells.
366 Next, given that vertebrate embryonic development is not deterministic and that variability exists
367 between embryos of the same genotype, we compared results between wild type embryos,
368 finding that LongAxis indeed allows us to detect differences between embryos of the same
369 genotype. Therefore, analysis of multiple embryos of the same genotype is necessary to
370 provide a complete quantitative picture of the phenotype range encompassed.

371 Finally, we returned to the biological question we initially sought to answer. *lama1* mutant
372 optic cups are comprised of misoriented retinal progenitors which are shorter and slightly less
373 elongated than their wild type counterparts. We had not previously detected the elongation
374 defect, likely due to combination of 2-dimensional analysis and small sample size. Misoriented
375 retinal progenitors appear to cluster together in domains of the optic cup, rather than being
376 scattered throughout the tissue randomly. We speculate that this is due to the ability of cells to
377 self-organize in the absence of extrinsic polarity cues. We did indeed detect and were able to
378 quantify variability between individual *lama1* mutant embryos, with one embryo exhibiting less
379 disruption to cell orientation than the other two. Did removal of the apical determinant *pard3*
380 rescue these phenotypes? Although certain single optical sections looked as though cells were
381 well-oriented toward the lens, 3-dimensional urchin plots demonstrate that cell orientation in

382 *lama1;MZpard3* double mutant optic cups is clearly not rescued; again, misoriented cells cluster
383 together in domains of the optic cup. Further, we detected a change in cell size and shape in
384 the double mutants: cells are larger and less elongated than their wild type or *lama1* single
385 mutant counterparts. The underlying cause of this change in cell size is unknown, but *pard3*
386 has been linked to regulation of proliferation in some systems (Costa et al., 2008); these
387 mechanisms will be interesting to explore moving forward.

388 LongAxis is currently optimized for the zebrafish optic cup, but could be modified for other
389 epithelial organs. Tissue organization is a crucial aspect of the development of numerous other
390 organs, including brain, ear, and gut. LongAxis is already potentially capable of cell morphology
391 quantification in these other systems; by modifying the code provided, cell orientation analysis
392 could be adapted for a different specific 3-dimensional structure of interest: for example, the
393 convergence point in the eye could be modified to be the midline plane in the developing brain.

394 As imaging technologies and approaches continue to improve our ability to visualize the
395 cellular basis of tissue assembly and morphogenesis, it is important that our analysis methods
396 also evolve to take advantage of this rich source of 3-dimensional quantitative information.
397 Tools such as LongAxis will help us connect molecular genetics to cell biology to uncover the
398 mechanisms underlying morphogenesis and development of the visual system and other organs
399 of interest.

400
401

402 **Experimental Procedures**

403

404 *Zebrafish husbandry and mutant/transgenic lines*

405 All zebrafish husbandry (*Danio rerio*) was performed under standard care conditions in
406 accordance with University of Utah Institutional Animal Care and Use Committee (IACUC)
407 Protocol approval (Protocol #18-02006). Embryos were raised at 28.5-30°C and staged
408 according to time post fertilization and morphology (Kimmel et al., 1995). Mutant lines were
409 previously described: *lama1^{UW1}* (Bryan et al., 2016; Semina et al., 2006); *pard3^{fh305}* (Blasky et
410 al., 2014). In all cases, maternal-zygotic *pard3* mutants (*MZpard3*) were used.

411 *lama1^{UW1}* genotyping protocol. A dCAPS strategy (Neff et al., 1998) was used with the
412 following primers: 5'
413 GCAGATGCAGCAACCACAGCCAGTCATGTGACCTGCACACCGCCAACACCT; 3'
414 GGCTTTCCCCTCTGATGACACGTAC. PCR annealing temperature, 58°. PCR products

415 were digested with DraIII, which cuts WT (231+47 bp), not mutant (278 bp). Digest products
416 were run on 3.2% Metaphor or 1% Metaphor/1% agarose gel.

417 *pard3*^{fh305} genotyping protocol. A CAPS strategy was used with the following primers: 5'
418 ATGGCTTCAGCAGTTTTAAGAAA; 3' ATGATTGGCACTGAGTGAAGAAC. PCR annealing
419 temperature, 61°. PCR products were digested with HpyCH4IV, which cuts mutant (87+68 bp),
420 not WT (155 bp). Digest products were run on 3.2% Metaphor or 1% Metaphor/1% agarose gel.

421

422 *RNA synthesis and injections*

423 Capped RNA was synthesized using a pCS2 template (pCS2-EGFP-CAAX) and the
424 mMessage mMachine SP6 kit (Ambion). RNA was purified (Qiagen RNeasy Mini Kit) and
425 ethanol precipitated. 150 pg RNA was injected into the cell of 1-cell embryos.

426

427 *Imaging*

428 Embryos were dechorionated at 24 hpf and embedded in 1.6% low melting point agarose (in
429 E2+gentamycin) in Delta T dishes (Bioprotechs (#0420041500C)). Images were acquired using a
430 Zeiss LSM710 or LSM880 laser scanning confocal microscope. E2+gentamycin was overlaid,
431 and the dish covered to prevent evaporation. All imaging was performed with a 40X water-
432 immersion objective (1.1 NA). Datasets were acquired with the following parameters:
433 1024x1024; 0.21 x 0.21 x 0.42 μm voxel size. The entire depth of the optic cup was imaged,
434 resulting in z-stacks of 340-480 slices. All imaging was of live embryos, to avoid distortions that
435 accompany tissue fixation.

436

437 *LongAxis MATLAB code*

438 The full LongAxis MATLAB code is available here with annotations:
439 www.kwan-lab.org/longaxis

440

441 *LongAxis Segmentation Validation*

442 Segmentation accuracy for all cells was scored manually, by selecting a subvolume, usually
443 containing 50-70 cells. Each cell in the subvolume was examined individually against xy/xz/yz
444 cutaways of the original image data to determine how well the segmentation matched the image
445 data. Accuracy was scored on a scale of 1-5, with 1-4 corresponding to how well the
446 segmentation matched the image data (1 = 90-100%; 2 = 70-90%; 3 = 50-70%; 4 = <50%), and
447 a score of 5 representing unsuccessful segmentation resulting in fused cells.

448

449 *Plots*

450 Density, violin (with box and whisker), and stacked bar plots were generated using the
451 ggplot2 package in R. Exponential decay equations were derived and plotted in R using the
452 self-starting asymptotic regression function (SSasymp). Exponential decay equations followed
453 the formula: $y(t) = y_f + (y_0 - y_f)e^{-\lambda t}$, where y is the number of excluded cells; y starts at y_0 and
454 decays towards y_f at rate λ .

455

456 *Statistics*

457 For comparisons of length, length-width ratio, and volume between wild type, *lama1* single
458 mutant, and *lama1;MZpard3* double mutant, data were compared using ANOVA, followed by
459 Tukey's test. For comparisons of distributions of angles of deviation, a two-sample Kolmogorov-
460 Smirnov test was carried out in R.

461

462

463

464 **Acknowledgments**

465 We are grateful to Bruce Appel for providing the *pard3^{fh305}* mutant line, and the University of
466 Utah Centralized Zebrafish Animal Resource for zebrafish husbandry. Thanks to members of
467 the Kwan lab for useful discussions and critical reading of the manuscript. This work was
468 supported by grants from the NEI/NIH (R01 EY025378, R01 EY025780) to K.M.K. C.D.B. was
469 supported by the University of Utah Developmental Biology Training Grant (NIH T32
470 HD007491).
471

472 **References**

- 473 Adams, J.C., Watt, F.M., 1993. Regulation of development and differentiation by the
474 extracellular matrix. *Development* 117, 1183-1198.
- 475 Adler, R., Canto-Soler, M.V., 2007. Molecular mechanisms of optic vesicle development:
476 complexities, ambiguities and controversies. *Dev Biol* 305, 1-13.
- 477 Bazin-Lopez, N., Valdivia, L.E., Wilson, S.W., Gestri, G., 2015. Watching eyes take shape. *Curr*
478 *Opin Genet Dev* 32, 73-79.
- 479 Blasky, A.J., Pan, L., Moens, C.B., Appel, B., 2014. *Pard3* regulates contact between neural
480 crest cells and the timing of Schwann cell differentiation but is not essential for neural crest
481 migration or myelination. *Dev Dyn* 243, 1511-1523.
- 482 Bryan, C.D., Chien, C.B., Kwan, K.M., 2016. Loss of laminin alpha 1 results in multiple structural
483 defects and divergent effects on adhesion during vertebrate optic cup morphogenesis. *Dev Biol*
484 416, 324-337.
- 485 Chow, R.L., Lang, R.A., 2001. Early eye development in vertebrates. *Annual review of cell and*
486 *developmental biology* 17, 255-296.
- 487 Costa, M.R., Wen, G., Lepier, A., Schroeder, T., Gotz, M., 2008. Par-complex proteins promote
488 proliferative progenitor divisions in the developing mouse cerebral cortex. *Development* 135, 11-
489 22.
- 490 Daley, W.P., Yamada, K.M., 2013. ECM-modulated cellular dynamics as a driving force for
491 tissue morphogenesis. *Curr Opin Genet Dev* 23, 408-414.
- 492 Frisch, S.M., Francis, H., 1994. Disruption of epithelial cell-matrix interactions induces
493 apoptosis. *The Journal of cell biology* 124, 619-626.
- 494 Fuhrmann, S., 2010. Eye morphogenesis and patterning of the optic vesicle. *Curr Top Dev Biol*
495 93, 61-84.
- 496 Hayes, J.M., Hartsock, A., Clark, B.S., Napier, H.R., Link, B.A., Gross, J.M., 2012. Integrin
497 alpha5/fibronectin1 and focal adhesion kinase are required for lens fiber morphogenesis in
498 zebrafish. *Mol Biol Cell* 23, 4725-4738.
- 499 Hendrix, R.W., Zwaan, J., 1975. The matrix of the optic vesicle-presumptive lens interface
500 during induction of the lens in the chicken embryo. *J Embryol Exp Morphol* 33, 1023-1049.
- 501 Hilfer, S.R., Randolph, G.J., 1993. Immunolocalization of basal lamina components during
502 development of chick otic and optic primordia. *Anat Rec* 235, 443-452.
- 503 Huang, J., Rajagopal, R., Liu, Y., Dattilo, L.K., Shaham, O., Ashery-Padan, R., Beebe, D.C.,
504 2011. The mechanism of lens placode formation: a case of matrix-mediated morphogenesis.
505 *Dev Biol* 355, 32-42.
- 506 Juliano, R.L., Reddig, P., Alahari, S., Edin, M., Howe, A., Aplin, A., 2004. Integrin regulation of
507 cell signalling and motility. *Biochemical Society transactions* 32, 443-446.
- 508 Kimmel, C.B., Ballard, W.W., Kimmel, S.R., Ullmann, B., Schilling, T.F., 1995. Stages of
509 embryonic development of the zebrafish. *Dev Dyn* 203, 253-310.
- 510 Kwan, K.M., 2014. Coming into focus: the role of extracellular matrix in vertebrate optic cup
511 morphogenesis. *Dev Dyn* 243, 1242-1248.
- 512 Lee, J., Gross, J.M., 2007. Laminin beta1 and gamma1 containing laminins are essential for
513 basement membrane integrity in the zebrafish eye. *Invest Ophthalmol Vis Sci* 48, 2483-2490.
- 514 Martin-Belmonte, F., Mostov, K., 2008. Regulation of cell polarity during epithelial
515 morphogenesis. *Current opinion in cell biology* 20, 227-234.
- 516 Martinez-Morales, J.R., Wittbrodt, J., 2009. Shaping the vertebrate eye. *Curr Opin Genet Dev*
517 19, 511-517.
- 518 Neff, M.M., Neff, J.D., Chory, J., Pepper, A.E., 1998. dCAPS, a simple technique for the genetic
519 analysis of single nucleotide polymorphisms: experimental applications in *Arabidopsis thaliana*
520 genetics. *Plant J* 14, 387-392.
- 521 Parmigiani, C., McAvoy, J., 1984. Localisation of laminin and fibronectin during rat lens
522 morphogenesis. *Differentiation* 28, 53-61.

- 523 Peterson, P.E., Pow, C.S., Wilson, D.B., Hendrickx, A.G., 1995. Localisation of glycoproteins
524 and glycosaminoglycans during early eye development in the macaque. *J Anat* 186 (Pt 1), 31-
525 42.
- 526 Semina, E.V., Bosenko, D.V., Zinkevich, N.C., Soules, K.A., Hyde, D.R., Vihtelic, T.S., Willer,
527 G.B., Gregg, R.G., Link, B.A., 2006. Mutations in laminin alpha 1 result in complex, lens-
528 independent ocular phenotypes in zebrafish. *Dev Biol* 299, 63-77.
- 529 Svoboda, K.K., O'Shea, K.S., 1987. An analysis of cell shape and the neuroepithelial basal
530 lamina during optic vesicle formation in the mouse embryo. *Development* 100, 185-200.
- 531 Tuckett, F., Morriss-Kay, G.M., 1986. The distribution of fibronectin, laminin and entactin in the
532 neurulating rat embryo studied by indirect immunofluorescence. *J Embryol Exp Morphol* 94, 95-
533 112.
- 534 Wakely, J., 1977. Scanning electron microscope study of the extracellular matrix between
535 presumptive lens and presumptive retina of the chick embryo. *Anat Embryol (Berl)* 150, 163-
536 170.
- 537 Webster, E.H., Jr., Silver, A.F., Gonsalves, N.I., 1984. The extracellular matrix between the
538 optic vesicle and presumptive lens during lens morphogenesis in an anophthalmic strain of
539 mice. *Dev Biol* 103, 142-150.
- 540 Yang, X.J., 2004. Roles of cell-extrinsic growth factors in vertebrate eye pattern formation and
541 retinogenesis. *Seminars in cell & developmental biology* 15, 91-103.

Figure 1. LongAxis workflow, image processing, and segmentation.

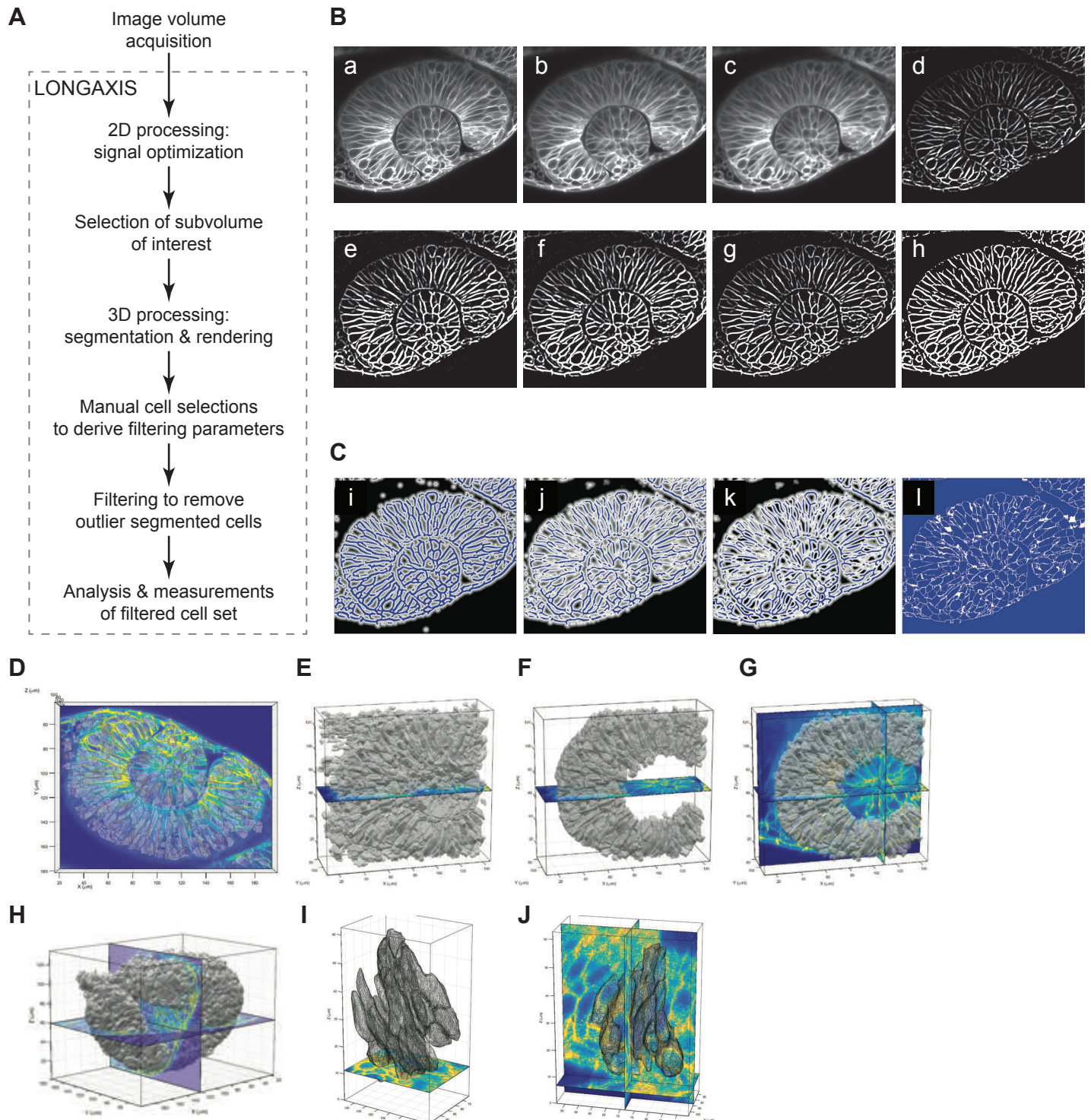


Figure 2. LongAxis data analysis and outputs.

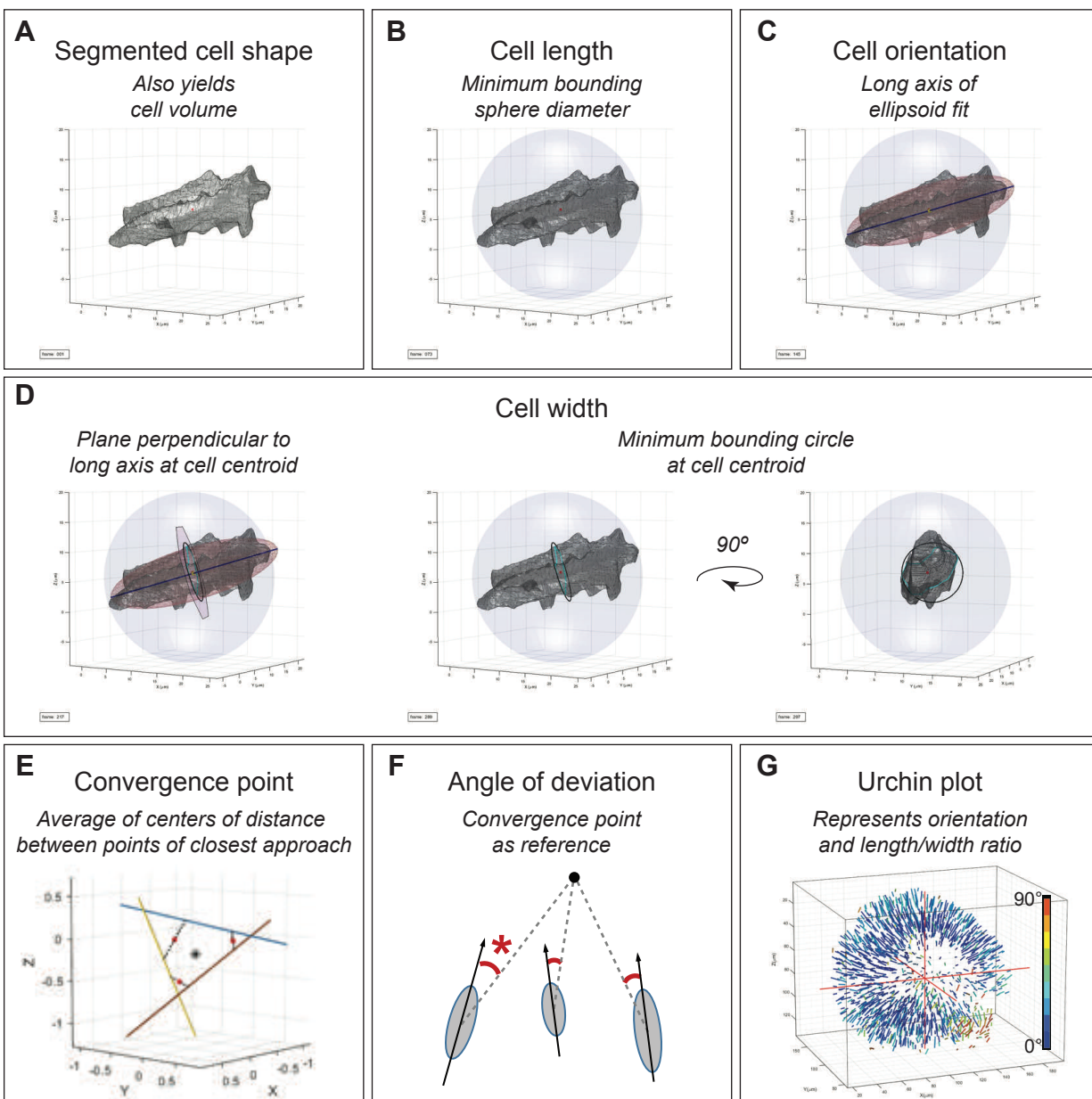


Figure 3. Filtering Analysis and Validation

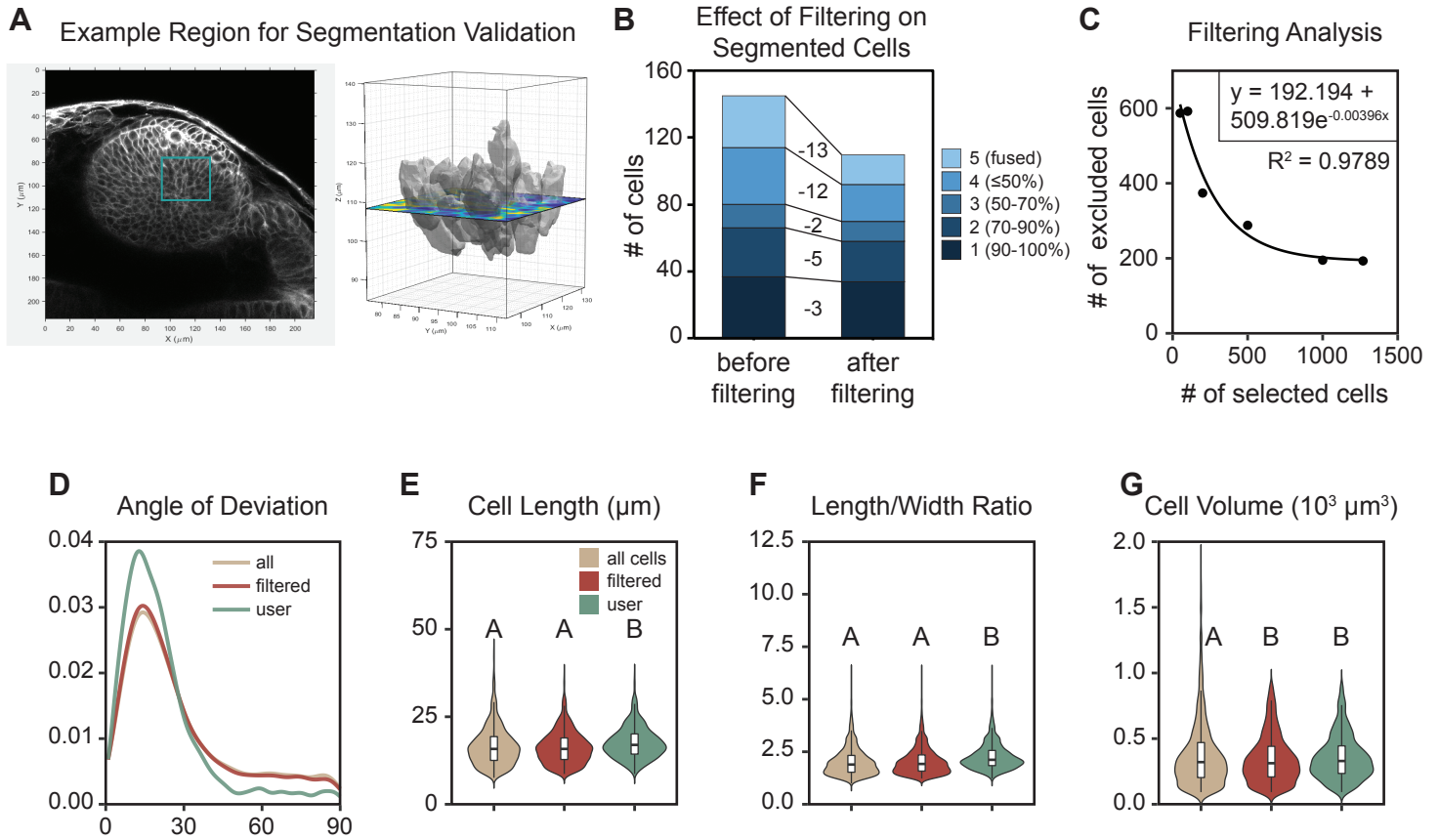


Figure 4

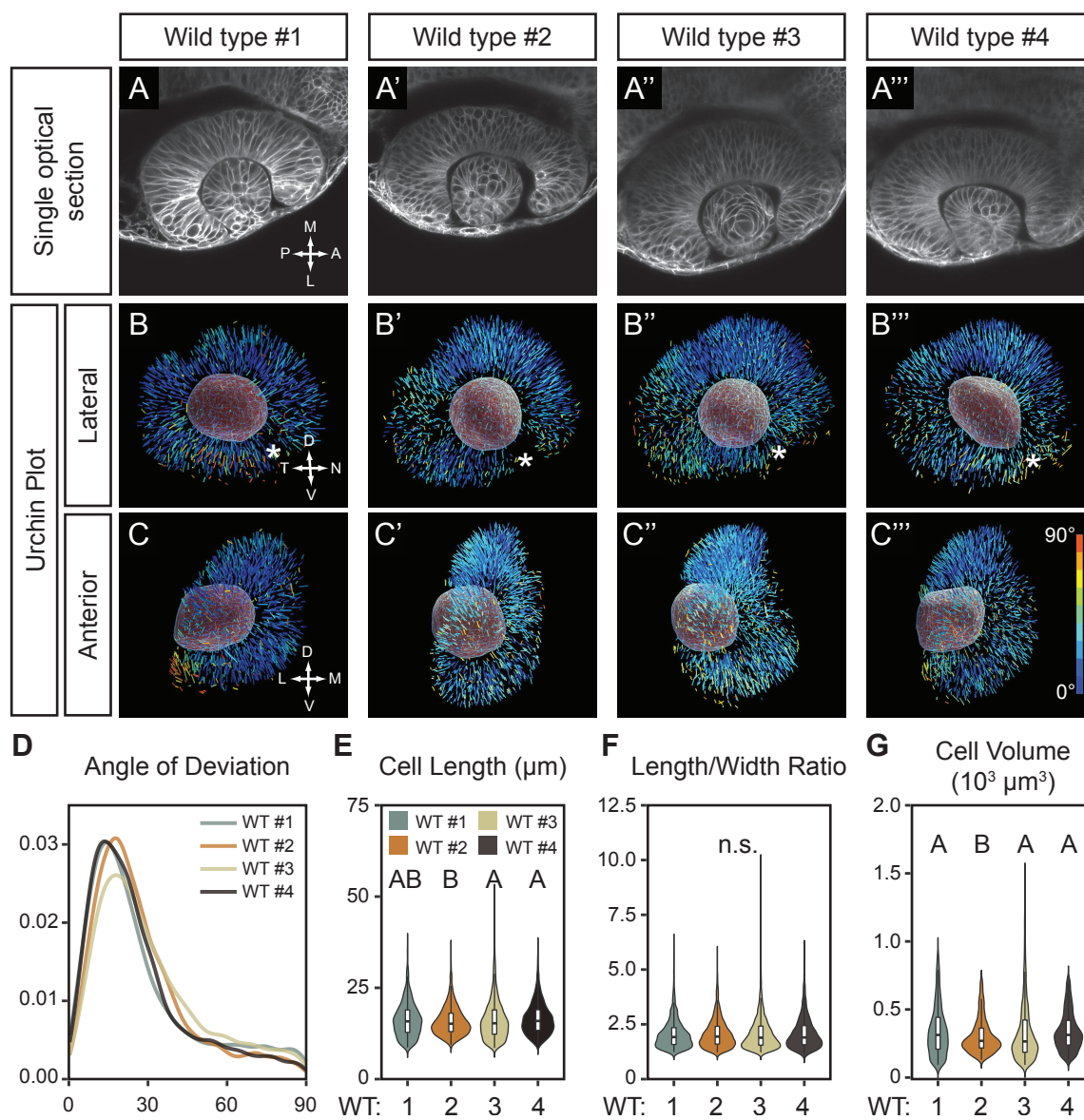


Figure 5

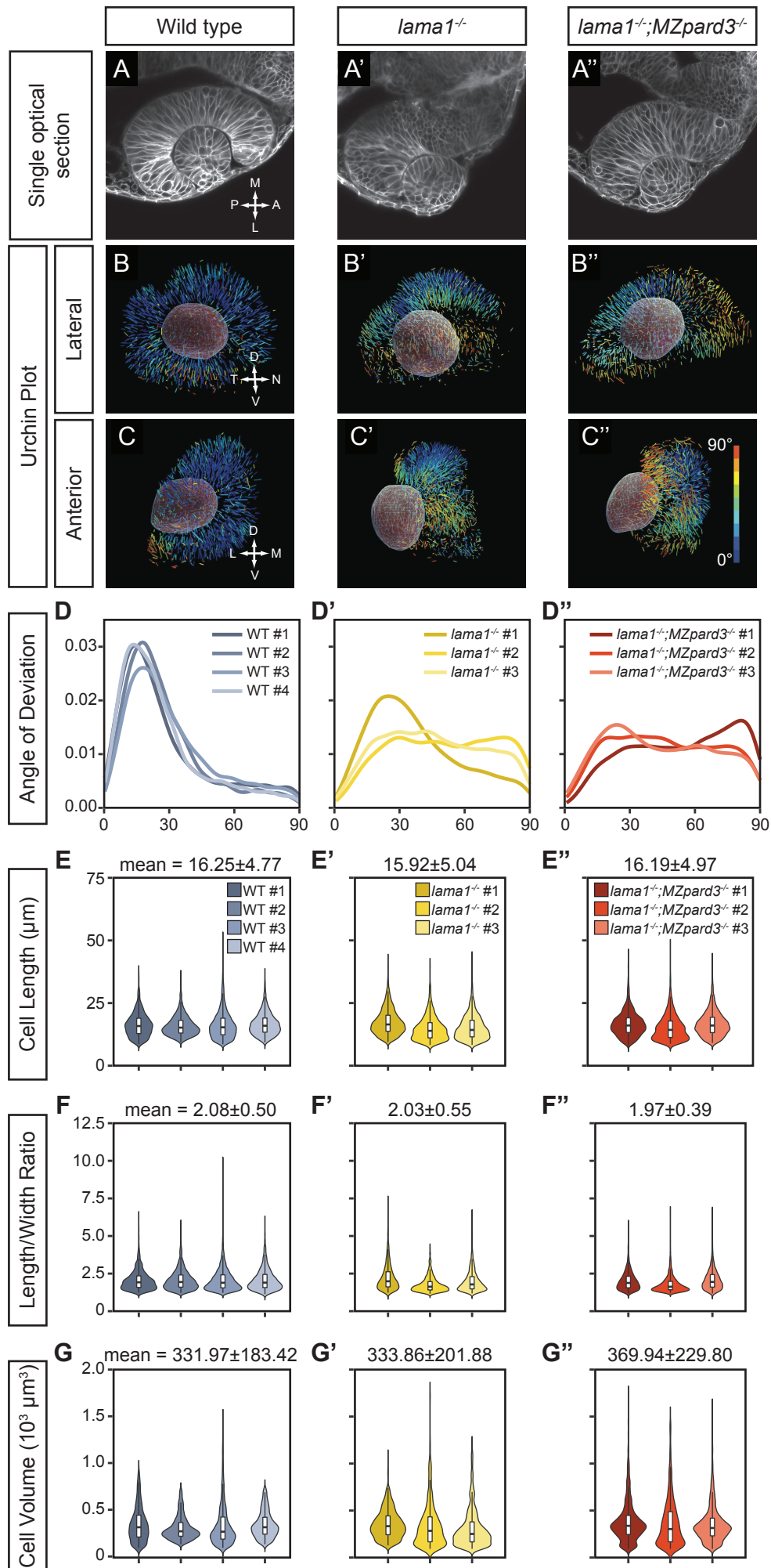


Figure S1.

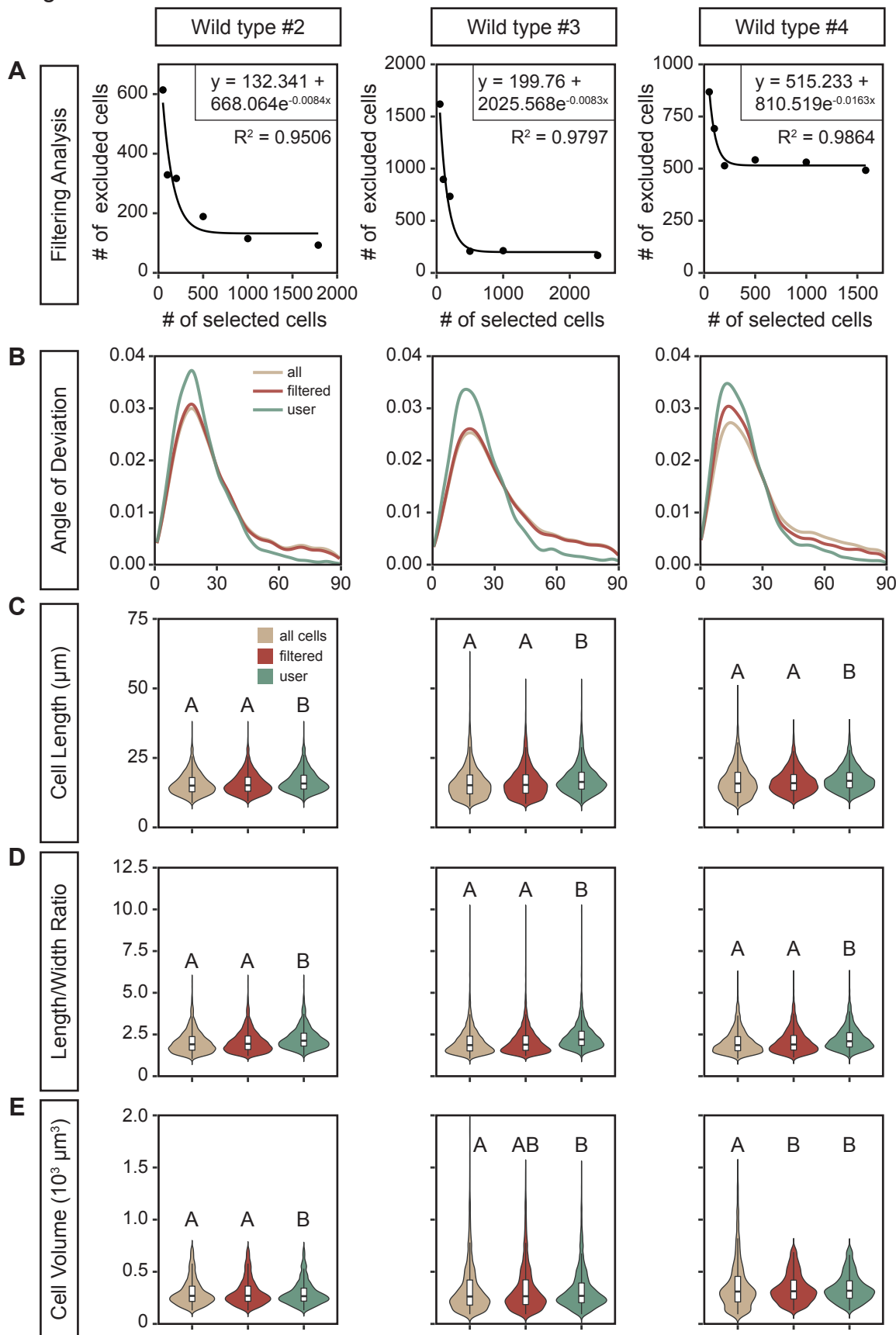


Figure S2.

